Model-Based Identification of Nanomechanical Properties in Atomic Force Microscopy: Theory and Experiments

Michael R. P. Ragazzon, J. Tommy Gravdahl, Kristin Y. Pettersen

Abstract—The ability of the atomic force microscope (AFM) to resolve highly accurate interaction forces, has made it an increasingly popular tool for determining nanomechanical properties of soft samples. Traditionally, elasticity is determined by gathering force-distance curves. More recently, dynamic properties such as viscoelasticity can be determined by relating the observables to sample properties, either by single- or multifrequency modulation of the cantilever. In this article, a model-based technique for resolving nanomechanical properties is presented. Both the sample and cantilever are represented by dynamic models. A recursive least squares method is then employed to identify the unknown parameters of the sample model, thus revealing its nanomechanical properties. Two sample models are presented in this article, demonstrating the ability to swap sample models to best suit the material being studied. The method has been experimentally implemented on a commercial AFM for online estimation of elastic moduli, spring constants and damping coefficients. Additionally, the experimental results demonstrate the capability of measuring time- or space-varying parameters using the presented approach.

Index Terms—mechanical properties, atomic force microscopy, parameter identification, dynamic models, biomedical systems

I. INTRODUCTION

ATOMIC force microscopy (AFM) is a versatile tool capable of imaging rigid and soft samples at nano- to micrometer resolutions [1]. In addition to determining the topography of a sample, it is capable of measuring tip-sample interaction forces in the piconewton range, due to its highly sensitive laser-cantilever setup as illustrated in Fig. 1. AFM enjoys many advantages over comparable techniques. In particular, it has the ability to measure forces accurately at high spatial resolution in most media, including air, water and solutions. These attributes have made AFM an increasingly popular tool for studying nanomechanical properties of materials in fields such as cell- and molecular biology, solid-state physics, and surface chemistry [2]–[4].

By measuring the static force response as the cantilever tip indents a soft sample, elastic properties of the sample can be revealed from the resulting force-distance curves [5]. In force-volume imaging mode [6], [7], indentations are repeated across the sample, which allows its elastic modulus to be spatially

M.R.P. Ragazzon and J.T. Gravdahl are with the Department of Engineering Cybernetics, NTNU, Norwegian University of Science and Technology, Trondheim, Norway. Email: {michael.remo.ragazzon, jan.tommy.gravdahl}@ntnu.no.

K.Y. Pettersen is with the Centre for Autonomous Marine Operations and Systems (NTNU AMOS), Department of Engineering Cybernetics, NTNU, Trondheim, Norway. Email: kristin.y.pettersen@ntnu.no.

resolved along the lateral axes. A variation to force-volume imaging includes the peakforce quantitative nanomechanical mode, which forcibly oscillates the cantilever at below resonance frequency, allowing for faster and higher-resolution gathering of force-distance curves [8], [9]. In HarmoniX and torsional harmonic modes [10], special cantilevers are used to induce a torsional force, allowing for the reconstruction of force-distance curves.

In order to obtain viscous and other dynamic properties of the sample, the time-history of the tip-sample interaction needs to be considered [11], [12]. Properties such as amplitude and phase can be gathered by modulating the cantilever near its resonance frequency, as in dynamic mode AFM [1], [13]–[15]. However, such observables are a property of the experimental setup and can not be considered consistent across experiments.

In an effort to relate the observables to material properties, early results demonstrated correlations between amplitude and elasticity, and between phase and viscosity [16]. More recently, considerable efforts have been placed toward revealing nanomechanical properties through higher-harmonics and multifrequency approaches [17]–[24]. These efforts typically involve relating the observables in either single- or multifrequency dynamic modulation to mechanical properties of the sample. However, these relations are often quite complicated and are still under development [25]. Furthermore, existing approaches are limited in terms of the properties that can be extracted from the sample, typically isolated to viscoelastic properties and their gradient along the depth axis. Avoiding such complicated relations, and allowing for additional properties to be identified, would be beneficial.

Using AFM to resolve mechanical properties has already opened up a new window into studying soft samples at the nano- to microscale. However, there is clearly room for improvements. Another approach, the dynamic indentation viscoelastic (DIVE) mode, was introduced in the previous work of the authors [26], based on preliminary results from [27], [28]. In DIVE mode, both the sample and cantilever are represented by separate dynamic models. By employing identification techniques from the control literature, the parameters of the dynamic sample model can be identified from the observable signals. The observables are mapped to the sample parameters using a recursive least squares method.

In order to spatially resolve nanomechanical properties, DIVE mode operates by indenting into the sample at regular intervals, laterally spaced across the scanning region. During the scan, the cantilever tip is modulated in order to gain dy-

namic information from the sample. Between each indentation, the cantilever is raised and moved in a raster pattern to the next indentation point, until the entire sample is covered. The cantilever is only moved in the lateral directions while the tip is completely retracted from the sample. The operation of DIVE mode is illustrated in Fig. 2.

In [26], the demonstration of DIVE mode was restricted to numerical results with the sample modeled as spring-damper elements. In this article, several aspects of the original work are expanded upon and experimental results are presented. In particular, (i) improvements are introduced to the system model, making it suitable for experiments. (ii) An additional sample model is introduced based on the Hertz contact model, allowing for online estimation of elastic moduli. (iii) A sufficient time interval during each indentation for guaranteed convergence of the sample parameters to any accuracy is derived. (iv) In order to implement the experiments, the parameter estimator is combined with a demodulator, an XYZ controller, and novel control logic implemented by a state machine. (v) Experimental results demonstrate the feasibility of the approach, using either of the two sample models, allowing for online estimation of spring constants, damping coefficients, and elastic moduli. Finally, (vi) experimental results additionally demonstrate identification of time-varying sample parameters using the presented approach.

Furthermore, in this article we present an upper bound on the exponential convergence of the parameter error, for the recursive least squares estimator in general. Preliminary results on this were presented in [29]. In this article, the results are extended by determining the estimation time interval for which the parameter error is guaranteed to have been reduced to some fraction of the initial error, after performing a covariance reset.

The modeling and identification approach taken by the DIVE mode, enjoys several advantages over comparable techniques. Because the sample and cantilever dynamics are separated, the complicated relationships between the observables and the sample properties are circumvented. Instead, the observable signals are fit to the sample model in a least squares sense. Furthermore, this separation makes it easy to swap out, or expand, the sample model for one which could better match the material, as demonstrated in this article. Additionally, since the technique employs a recursive method, it can be implemented online and allows for observing time- or space-varying changes of the parameters.

The article is organized as follows. In Sec. II the cantilever and sample dynamics are modeled. The estimation procedure for the unknown sample parameters is presented in Sec. III. Implementation details of the approach are given in Sec. IV. System identification of the cantilever model and tuning of the parameter estimator is demonstrated in Sec. V. Experimental results are presented in Sec. VI. Finally, conclusions are drawn in Sec. VII.

II. SYSTEM MODELING

In this section, the dynamics governing the AFM cantilever interacting with the sample are established. This is later used for developing appropriate parameter identification laws for the sample mechanical properties.
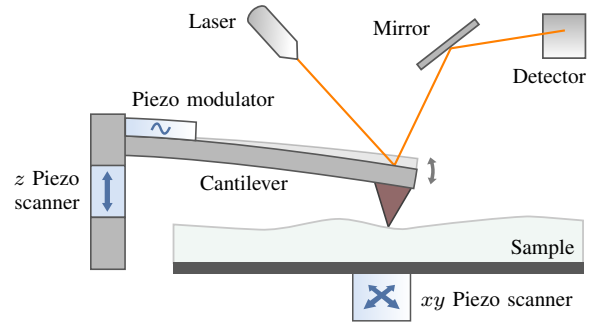

Fig. 1: AFM dynamic mode setup.

The following is based on [26]. However, in the original work, modulation of the cantilever was generated by modulating the z-scanner. In a typical AFM setup, this scanner is severely bandwidth-limited, and unable to oscillate the cantilever near its resonance frequency. In this work, modifications are introduced by instead employing the piezo modulator typically used in dynamic modes of AFM. Additionally, in the original work, only a spring-damper model was used to describe the sample. In this work, contact mechanics are considered, resulting in a second, nonlinear dynamic sample model.

A. System overview

The coordinate system in the xz-plane of the AFM cantilever and sample is illustrated in Fig. 3. The position of the tip along the xyz-axes is denoted by (X, Y, Z). The vertical tip position Z, the cantilever deflection D, and the cantilever tip rest position Z_0 are related by

$$Z = Z_0 + D. \tag{1}$$

The deflection D is typically measured through a photodetector setup, and assumed available. The signal is positive along the z-direction with its origin placed at Z_0.

The interaction between the various components of the system is shown in Fig. 4, with corresponding inputs and outputs assumed available. The cantilever dynamics are subject to an external tip-sample interaction force F_{ts}, as well as a modulating input force F_{mod}. The resulting cantilever deflection, as well as the z-actuator position, determines the tip position Z. As the tip indents the sample at depth δ, restoration and viscous forces from the sample are acting on the tip. The cantilever dynamics and contact forces are discussed in the following sections.

The xy- and z-actuators are often implemented by piezo scanners along each axis, as illustrated in Fig. 1. These actuators typically display vibration dynamics as well as nonlinear effects, such as creep and hysteresis [30]–[32]. However, these dynamics are not considered in this work, instead, any disturbances are assumed suppressed through feedback control. Such control schemes have been the topic of a large amount of research [33]–[36]. The signals X, Y, Z_0 are considered measurable and controllable through actuators on each axis, by the signals U_x, U_y, U_z, respectively.
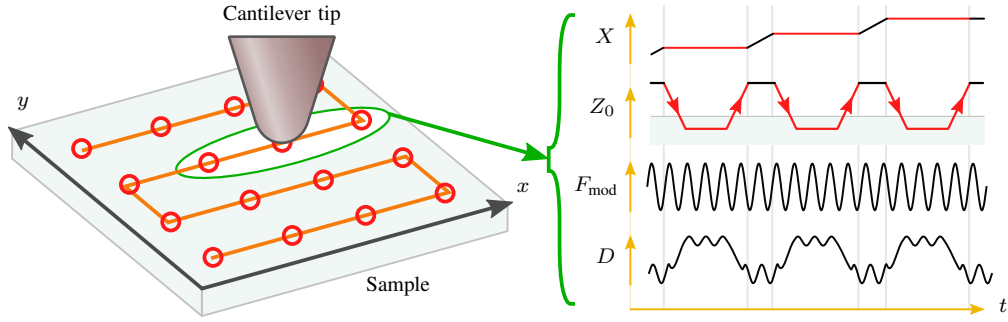
Fig. 2: Operation of DIVE mode in AFM, for a 4×4-resolution image. The tip is indented into the sample at each red circle. The lateral movement is paused during indentation. During the entire procedure, the cantilever is oscillated using the piezo modulator, which enables identification of dynamical properties such as viscosity.
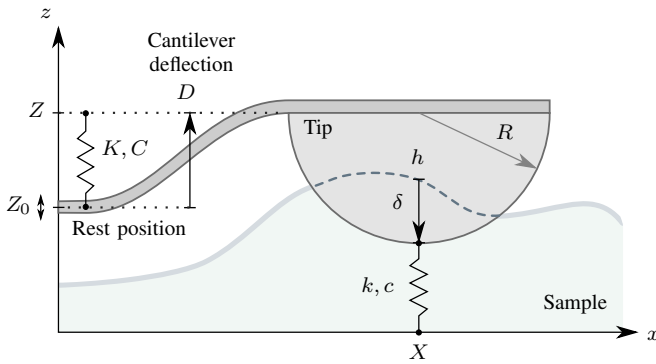

Fig. 3: AFM cantilever interacting with the sample. The deflection and tip size is exaggerated for illustration purposes.
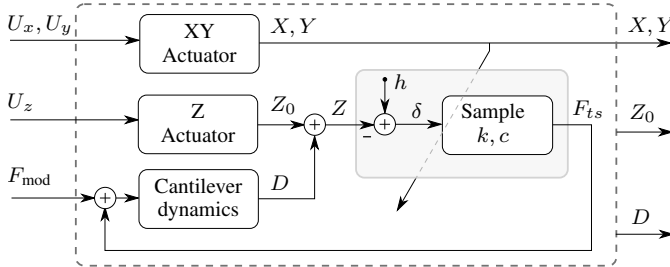

Fig. 4: Plant dynamics and corresponding inputs and outputs. The sample properties – here k, c, h – are to be identified from the available signals.

B. Cantilever dynamics

The cantilever dynamics can be approximated by its first resonance mode [13], resulting in the spring-damper system

$$M\ddot{D} + KD + C\dot{D} = F_{\text{mod}} + F_{\text{ts}} \tag{2}$$

where M is the effective mass of the cantilever [37], K, C are the cantilever spring and damping constants respectively, F_{mod} is the modulation force from the piezo modulator, and F_{ts} is the force from the sample acting on the cantilever tip. Furthermore, the cantilever resonance angular frequency is denoted by ω_0.

C. Indentation depth

The indentation depth of the tip δ can be determined during the approach phase for each indentation into the sample. The indentation is given by

$$\delta = h - Z \tag{3}$$

where h is the sample topography at the current tip position. As the origin of the topography is arbitrarily placed along the z-axis, any constant terms, such as the tip radius and height, can safely be disregarded. The topography h is found by measuring and recording the first point of contact during approach, thus δ is assumed known. The detection scheme for the first point of contact is described in Sec. IV. Once detected, the topography h at the current indentation is set and used in the relevant computations.

D. Contact mechanics

As the cantilever approaches the sample, two different regimes determine the nature of the tip-sample interaction. During approach (non-contact), the interaction force can be described using the Lennard-Jones potential [38]. As the tip comes in contact with the sample and starts indenting it, the mechanical response of the sample due to its deformation determines the interaction. The latter interaction is of main interest in this work.

Traditionally, the Hertz contact model has been widely used in the AFM community to describe elasticity of soft samples [16], [39]. This approach assumes small indentations, no friction, and continuous, non-conforming surfaces. For a spherical tip with radius R indenting into an elastic half-space, the contact force as a function of indentation δ is given by

$$F_{\text{Hertz}} = \tfrac{4}{3} E^* R^{\frac{1}{2}} \delta^{\frac{3}{2}} \tag{4}$$

where

$$E^* = \left(\frac{1 - \nu_{\text{tip}}^2}{E_{\text{tip}}} + \frac{1 - \nu^2}{E} \right)^{-1} \tag{5}$$

and ν_{tip}, ν are the Poisson ratios of the tip and sample, respectively, and E_{tip}, E are the elastic moduli of the tip and

sample. Since the cantilever tip is made of a stiff material, it can safely be assumed that $E_{\text{tip}} \gg E$, which simplifies (5) to

$$E^* = \frac{E}{1 - \nu^2}. \tag{6}$$

In the following, two separate models are presented for modeling the sample. The first one is a linear spring-damper model, while the second is based on the nonlinear Hertz model with an additional viscous term. Using two such models demonstrate that the presented approach can operate with various material descriptions, from a simple one which emphasizes implementation simplicity, to increasingly complex descriptions emphasizing accuracy.

E. Sample model $\mathcal{A}$: Spring-damper

A simplified approach to the sample interaction is achieved through modeling the sample by a spring-restoration force and a damper. This is equivalent to the Kelvin-Voigt model, considered one of the simpler models for viscoelasticity [3]. This model effectively captures viscoelastic effects such as creep, but may result in widely varying parameters due to being dependent on the frequency or time scale of the experiment. Additionally, due to the linearity of the elastic component of the model, the spring constant will change with depth, as well as the radius of the tip. The advantage of this approach is the simplicity of the equations, especially with regards to the linearity in terms of the indentation depth. The interaction force is given by

$$F_{\text{ts}}^{\mathcal{A}} = k\delta + c\dot{\delta} \tag{7}$$

where k is the spring constant, c is the damping coefficient, and δ is the indentation of the tip into the sample.

In the context of the Hertz contact model, the spring constant will change with the indentation depth, thus $k = k(\delta)$. If the spring constant is already known, the elastic modulus can be found offline by using (4), (6) and Hooke's law $F_{\text{Hooke}} = k\delta$, which gives

$$E = \tfrac{3}{4}k(1 - \nu^2)R^{-\frac{1}{2}}\delta^{-\frac{1}{2}}. \tag{8}$$

F. Sample model $\mathcal{B}$: Modified Hertz model

An alternative implementation of the sample model is obtained by directly using the Hertz contact model (4),(6). By supplementing this approach with a linear damping force as in the Kelvin-Voigt model, a viscoelastic model of the sample is obtained. The resulting tip-sample interaction force is given by

$$F_{\text{ts}}^{\mathcal{B}} = E'\delta^{\frac{3}{2}} + c\dot{\delta} \tag{9}$$

$$E = \tfrac{3}{4}R^{-\frac{1}{2}}(1 - \nu^2)E' \tag{10}$$

where E is the elastic modulus of the sample, E' is the variable identified by the parameter estimator and proportional to the elastic modulus, R is the cantilever tip radius, and ν is the Poisson ratio of the sample – typically $\nu = 0.5$ for soft and biological samples [40]. The elastic modulus found by this approach should be invariant in terms of indentation depth, as long as the assumptions of the Hertz contact model hold.

III. PARAMETER IDENTIFICATION

In this section, an online estimation scheme for identification of the unknown sample parameters, k, c, E, is established. The cantilever deflection D and indentation depth δ are considered known signals during estimation, while the cantilever dynamics from the previous section, represented by the parameters M, K, C, are considered fixed during experiments.

First, the system dynamics are rewritten in a parametric form, suitable for estimation. Here, the two sample models $\mathcal{A}$ and $\mathcal{B}$ are treated separately. The two models are then applied in a generic recursive least squares estimator for identifying the unknown parameters. Finally, convergence of the parameter estimates is discussed.

A. Parametric system model

For the spring-damper model $\mathcal{A}$, by applying the interaction force (7) to the cantilever model (2), the equations can be rearranged and rewritten in the complex s-domain as

$$Ms^2D + CsD + KD - F_{\text{mod}} = (cs + k)\delta. \tag{11}$$

Defining

$$w' \triangleq Ms^2D + CsD + KD - F_{\text{mod}} \tag{12}$$

the system (11) can be rewritten in parametric form as

$$w' = \begin{bmatrix} c \\ k \end{bmatrix}^T \begin{bmatrix} s\delta \\ \delta \end{bmatrix} \tag{13}$$

$$= \boldsymbol{\theta}_{\mathcal{A}}^T \boldsymbol{\phi}_{\mathcal{A}}' \tag{14}$$

where $\boldsymbol{\theta}_{\mathcal{A}}$ is the unknown parameter vector to be estimated and $\boldsymbol{\phi}_{\mathcal{A}}$ is the known signal vector.

Following the same procedure for the Hertz model $\mathcal{B}$, the interaction force (7) and cantilever model (2) can be written as

$$Ms^2D + CsD + KD - F_{\text{mod}} = cs\delta + E'\delta^{1.5}. \tag{15}$$

By using (12), the system can be written as

$$w' = \begin{bmatrix} c \\ E' \end{bmatrix}^T \begin{bmatrix} s\delta \\ \delta^{1.5} \end{bmatrix} \tag{16}$$

$$= \boldsymbol{\theta}_{\mathcal{B}}^T \boldsymbol{\phi}_{\mathcal{B}}' \tag{17}$$

which gives the parametric formulation of the second sample model.

B. Filtered system equations

In order to avoid pure differentiation of the signals w', ϕ_i' in (14), (17), both sides of each equation are filtered by a second-order low-pass filter such as $1/\Lambda(s) = 1/(\tau s + 1)^2$,

$$\frac{w'}{\Lambda} = \boldsymbol{\theta}_i^T \frac{\phi_i'}{\Lambda} \tag{18}$$

$$w = \boldsymbol{\theta}_i^T \boldsymbol{\phi}_i \tag{19}$$

for $i \in \{\mathcal{A}, \mathcal{B}\}$. Since w' is of degree two, and ϕ_i' is of degree one, using a second-order low-pass filter makes the transfer functions w, ϕ_i proper and thus implementable.

This linear parametric form is suitable for implementation of various parameter estimation schemes, such as given in [41]. The objective of the estimator is thus to find the unknown $\boldsymbol{\theta}_i$ given the known signals w and ϕ_i.

C. Parameter estimator

Several estimation methods for the systems (14),(17) can be employed with similar stability and convergence properties. We have chosen the least squares method with forgetting factor from [41], due to its greater ability to suppress measurement noise over many comparable techniques. Furthermore, because of the slowly varying nature of the parameters, a forgetting factor is useful. The method is restated here for completeness,

$$\widehat{w} = \widehat{\boldsymbol{\theta}}^T \boldsymbol{\phi} \tag{20}$$

$$\varepsilon = (w - \widehat{w})/m^2 \tag{21}$$

$$m^2 = 1 + \alpha \boldsymbol{\phi}^T \boldsymbol{\phi} \tag{22}$$

$$\dot{\widehat{\boldsymbol{\theta}}} = \mathbf{P} \varepsilon \boldsymbol{\phi} \tag{23}$$

$$\dot{\mathbf{P}} = \beta \mathbf{P} - \mathbf{P} \frac{\boldsymbol{\phi} \boldsymbol{\phi}^T}{m^2} \mathbf{P} \tag{24}$$

$$\mathbf{P}(0) = \mathbf{P}_0 \tag{25}$$

where the parameter estimate vector $\widehat{\boldsymbol{\theta}} = \widehat{\boldsymbol{\theta}}_i$, and signal vector $\boldsymbol{\phi} = \boldsymbol{\phi}_i$ are implemented for some $i \in \{\mathcal{A}, \mathcal{B}\}$. Additionally, α is a positive constant, typically unity, $\beta > 0$ is the main tunable for the convergence speed of the estimates, and $\mathbf{P} \in \mathbb{R}^{2 \times 2}$ is the covariance matrix.

The sample rate needs to be sufficiently high to achieve numerical stability of the estimator. If numerical instability is observed, the estimator gain β can be reduced to ease the numerical demands. A recommended lower limit on the sample rate can be found by considering the cantilever oscillating near its resonance frequency $f_0 = \omega_0/(2\pi)$. To capture information at this frequency, by the Nyquist criterion, the sample rate needs to be at least twice this frequency, giving a lower limit of $f_{s,\min} = 2f_0$. However, the sample rate may need to be increased further to achieve numerical stability.

D. Convergence of parameters

The least squares estimator guarantees convergence of the error ε to zero, given constant parameters $\boldsymbol{\theta}$. However, for the parameter vector $\widehat{\boldsymbol{\theta}}$ to converge to $\boldsymbol{\theta}$, which is of prime importance in parameter identification, the signal vector $\boldsymbol{\phi}$ needs to be persistently exciting (PE). Indeed, this is a sufficient condition for exponential convergence of $\widehat{\boldsymbol{\theta}} \to \boldsymbol{\theta}$ [41].

Definition 1 (Persistency of excitation). The signal vector $\boldsymbol{\phi}$ is said to be PE if there exist constants, $\alpha_0, \alpha_1, T_{\mathrm{p}} > 0$ such that

$$\alpha_0 \mathbf{I} \leq \frac{1}{T_{\mathrm{p}}} \int_t^{t+T_{\mathrm{p}}} \boldsymbol{\phi} \boldsymbol{\phi}^T d\tau \leq \alpha_1 \mathbf{I}, \quad \forall t \geq 0, \tag{26}$$

where $\mathbf{I}$ is the identity matrix and α_0 is known as the level of excitation.

For a modulating cantilever, that is, by using a sinusoidal input signal

$$F_{\mathrm{mod}} = A' \sin(\omega_0 t) \tag{27}$$

for some amplitude A', the signal vector is PE as demonstrated later. Thus, in dynamic mode AFM the parameters will convergence in exponential time.

The estimation scheme guarantees exponential convergence only for constant parameters. However, exponential convergence in the constant parameter case, guarantees some degree of tracking even for slowly-varying parameters [42]. Thus, the estimation scheme can be used to track sample mechanical changes over time, or as a function of another signal, such as the indentation depth. To capture more rapid changes in parameters, e.g. during indentation, one could reduce the scanning speed or increase the gain of the parameter estimator.

E. Estimation time interval for convergence

Although the PE property guarantees exponential convergence of the parameters, even exponential convergence can be slow. In DIVE mode AFM, the parameters can be assumed to take on new constant values at regular intervals from one indentation to the next. The question then remains, how long does the parameter estimator need to run during a given indentation in order to guarantee convergence to some specified error? This topic was investigated in detail in [29] for the general case of the recursive least squares method. Some results are restated here and extended for the case of covariance reset between each interval. A covariance reset, that is, setting $\mathbf{P}(t_0) = \mathbf{P}_0$ at some time t_0, is used as it allows for tighter error bounds and thus faster guaranteed convergence time.

In the following theorem, an upper limit on the parameter error is given. Let the parameter estimation error be given by $\widetilde{\boldsymbol{\theta}} = \widehat{\boldsymbol{\theta}} - \boldsymbol{\theta}$.

Theorem 1. *Let $m, \boldsymbol{\phi} \in \mathcal{L}_\infty$, $\boldsymbol{\phi}$ be PE, and $\boldsymbol{\theta}$ constant. Then, by a covariance reset at time t_0 such that $\mathbf{P}(t_0) = \mathbf{P}_0$, the least squares algorithm guarantees*

$$\left| \widetilde{\boldsymbol{\theta}}(t) \right| \leq a e^{-\lambda(t-t_0)} \left| \widetilde{\boldsymbol{\theta}}(t_0) \right|, \quad \forall t \geq t_0 \tag{28}$$

for any $t_0 \geq 0$, where the constants $a > 1, \lambda > 0$ are given by

$$a = \sqrt{\frac{\gamma_2}{\gamma \lambda_{\min}(\mathbf{P}_0)}}, \quad \lambda = -\frac{\ln \gamma}{2 T_p}, \tag{29}$$

where

$$\gamma = \frac{1 - \mu}{1 + \beta T_p} \tag{30}$$

$$\mu = \frac{\alpha_0 T_p \gamma_1}{2 \bar{m}^2 + \bar{\phi}^4 T_p^2 \gamma_2^2} \tag{31}$$

$$\gamma_1 = \left(\lambda_{\min}(\mathbf{P}_0)^{-1} + (\alpha\beta)^{-1} \right)^{-1} \tag{32}$$

$$\gamma_2 = \max \left\{ \frac{\bar{m}^2}{\alpha_0 T_p}, \lambda_{\max}(\mathbf{P}_0) \right\} e^{\beta T_p}. \tag{33}$$

Additionally, $\bar{m}^2 = \sup_t m^2(t)$, $\bar{\phi} = \sup_t |\boldsymbol{\phi}|$ and $\lambda_{\min}(\cdot)$, $\lambda_{\max}(\cdot)$ denote the minimum and maximum eigenvalue, respectively.

Proof: This theorem is a reformulation of [29, Theorem 1]. $\square$

Using the previous theorem, a time interval T can then be found such that the parameter error is guaranteed to be reduced to some fraction Q of the initial error.

Corollary 1. *Given that the assumptions of Theorem 1 are satisfied. Then, for any $0 < Q < 1$, the recursive least squares algorithm guarantees that within the time interval*

$$T = \frac{1}{\lambda} \ln \frac{a}{Q} \qquad (34)$$

the parameter error has been reduced to the fraction Q, that is

$$\frac{\left|\widetilde{\boldsymbol{\theta}}(T + t_0)\right|}{\left|\widetilde{\boldsymbol{\theta}}(t_0)\right|} \leq Q \qquad (35)$$

Proof: Let $T = t - t_0$, and rewrite (28) as

$$\left|\widetilde{\boldsymbol{\theta}}(T + t_0)\right| \leq a e^{-\lambda T} \left|\widetilde{\boldsymbol{\theta}}(t_0)\right|, \quad \forall T \geq 0. \qquad (36)$$

Note that, since $a > Q$ and $\lambda > 0$, we have $T > 0$ using (34), thus, the condition $T \geq 0$ in (36) is automatically satisfied. Now, inserting for T from (34) gives

$$\left|\widetilde{\boldsymbol{\theta}}(T + t_0)\right| \leq a e^{-\lambda \frac{1}{\lambda} \ln \frac{a}{Q}} \left|\widetilde{\boldsymbol{\theta}}(t_0)\right| \qquad (37)$$

$$\leq a \frac{Q}{a} \left|\widetilde{\boldsymbol{\theta}}(t_0)\right| \qquad (38)$$

$$\leq Q \left|\widetilde{\boldsymbol{\theta}}(t_0)\right|. \qquad (39)$$

which confirms (35). $\qquad \square$

As long as the PE parameters are known, specifically α_0, T_p from (26), then the time interval T can be found using (29) and (34).

IV. IMPLEMENTATION

The control logic and parameter estimator is implemented according to the block diagram shown in Fig. 5. The implementation details of the various components are discussed in the following.

A. State machine and parameter estimator

The state machine controls the logic of the operation. Its procedure is summarized in Fig. 6 and the following:

1) Lower the cantilever until indenting into the sample, and record the initial point of contact h (topography).
2) Pause the vertical movement of the cantilever when the mean deflection reaches some D_{max}.
3) Enable the parameter estimator. The duration of this step should be sufficient to guarantee convergence of the parameters as discussed later.
4) Raise the cantilever until it is free from the sample.
5) Move the cantilever in the lateral directions to the next indentation coordinate.

The above procedure is repeated $n \times n$ times for each indentation laterally spaced across the sample, where n determines the resolution of the resolved nanomechanical properties. The parameter estimator implements (20)–(25) for either sample model $\mathcal{A}$ or $\mathcal{B}$. Between each indentation, all internal states of the parameter estimator are reset.

B. Demodulator

The cantilever deflection signal is demodulated using a digital Lyapunov filter which provides the amplitude, phase and mean of the signal [43]. This demodulator has been compared to state-of-the-art techniques and demonstrates a high performance with simplicity of implementation [44]. The demodulator is exclusively used for:

- Determination of the initial point of contact with the sample during the approach phase – that is, the topography.
- Acquisition of the amplitude and phase for offline data analysis purposes.

Thus, only the state machine makes use of the demodulated signals. Contrarily, the parameter estimator rather uses the oscillating signals directly. Therefore, the performance of the demodulator does not directly influence the identified parameters.

The demodulator is implemented as

$$\dot{\widehat{\boldsymbol{x}}} = \boldsymbol{\Gamma} \boldsymbol{c} (D - \widehat{D}), \qquad (40)$$

$$\widehat{D} = \boldsymbol{c}^T \widehat{\boldsymbol{x}}, \qquad (41)$$

where the constant diagonal matrix $\boldsymbol{\Gamma} = \mathrm{diag}(\gamma_a, \gamma_a, \gamma_b)$, and $\gamma_a, \gamma_b > 0$ determine the bandwidth of the demodulation and the mean estimate, respectively. Furthermore, the state vector $\widehat{\boldsymbol{x}}$ and quadrature signal vector $\boldsymbol{c}$ are given by

$$\widehat{\boldsymbol{x}} = [\hat{x}_1, \, \hat{x}_2, \, \hat{x}_3]^T, \qquad (42)$$

$$\boldsymbol{c} = [\sin(\omega_0 t), \, \cos(\omega_0 t)]^T. \qquad (43)$$

The deflection amplitude D_A, phase D_φ, and mean $\bar{D}$ can then be recovered from

$$D_A = \sqrt{\hat{x}_1^2 + \hat{x}_2^2}, \qquad (44)$$

$$D_\varphi = \mathrm{atan2}\left(\hat{x}_2, \hat{x}_1\right), \qquad (45)$$

$$\bar{D} = \hat{x}_3, \qquad (46)$$

where $\mathrm{atan2}(\cdot)$ is the four-quadrant inverse tangent function.

The Lyapunov filter requires an exact knowledge of the frequency ω_0 of the modulated signal. The frequency is determined by the applied modulation signal F_{mod} from (27). Thus, by feeding this signal into the demodulator, the frequency will match trivially.

C. XYZ Controller

The XYZ controller positions the cantilever as commanded by the state machine. The controller takes the rate of movement along each axis, dX, dY, dZ, as reference, and positions the cantilever/sample accordingly.

Hysteresis and creep in the lateral piezo scanners can negatively influence the results. E.g., if the tip moves toward an area of higher topography during an indentation in DIVE mode, the value of the initial contact point would become invalid, and result in lower or even negative indentation depth values. This would introduce an error or completely invalidate the estimated parameters, especially for stiff samples and steep topography. In order to suppress such occurrences, a feedback PI-controller is implemented for accurate positioning along the lateral axes.
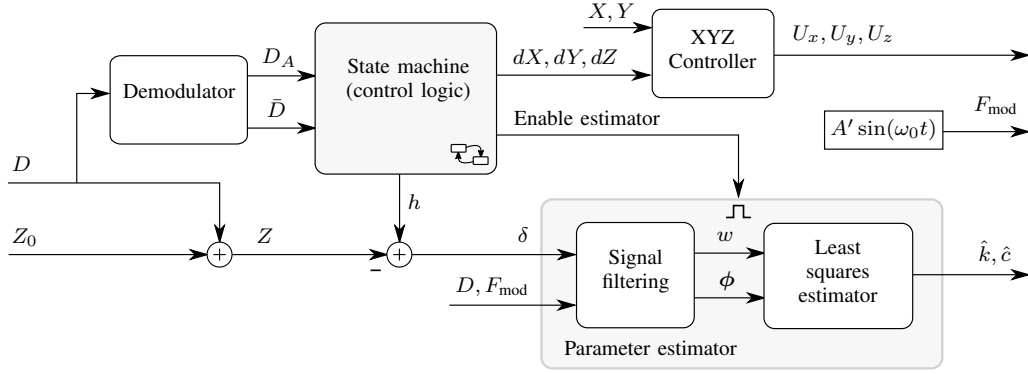
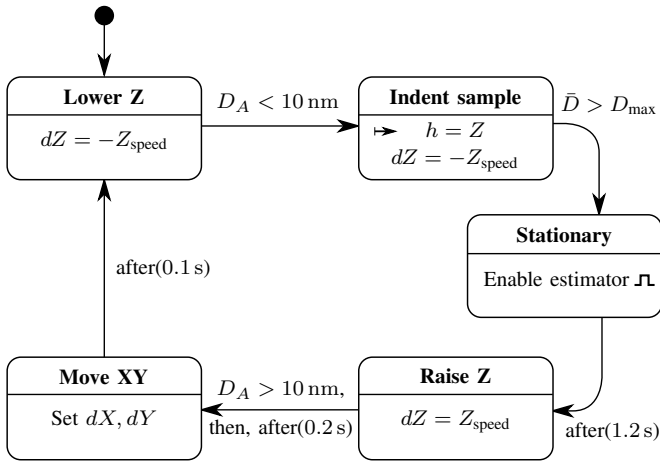Fig. 5: Block diagram of the control logic and parameter estimator.

Fig. 6: State machine controlling the overall operation of the procedure. One cycle represents a single indentation and is repeated for each pixel across the sample. The initial state is given by '•', while '↦' represents entry action. For other actions, their signals are reset to zero at state exit.

The vertical (z-axis) scanner on the other hand, is implemented using feedforward only. This scanner also displays hysteresis and creep. However, the effects along this axis are negligible as the recorded initial contact point is still valid. This leads to a correct measurement of indentation depth, and the estimated parameters remain valid even when the sample creeps in the vertical direction.

D. Other considerations

1) Contact point detection: In order to determine the depth of the cantilever during indentation, first the point of contact with the sample must be detected. This additionally serves as a measurement of the topography h at the current lateral position. A rigorous contact point detection can be challenging, especially for soft samples with strong surface forces [5]. During approach, attractive forces can result in a jump to contact, possibly causing sample indentation in addition to adhesion forces. For these reasons, there is no simple solution to determining the contact point. In our experiments the contact point was determined by the deflection amplitude

becoming less than some predetermined value, chosen as $D_A < 10$ nm. When this condition is reached, the topography is determined from the current vertical tip position, as detailed in Fig. 6.

2) Calibration: All signals are converted to SI units. For accurate indentation values, the deflection and vertical positioning need to be well calibrated. The vertical positioning can be calibrated by performing a scan over a rigid sample with a known step height. The deflection can be calibrated by performing an indentation into a rigid sample with the same cantilever as used in the experiment, and comparing this to the previously calibrated vertical positioning.

3) Deflection creep: It was observed that the resting, static deflection point of the cantilever creeped slowly over time. This also appeared to change the deflection calibration over time. This is believed to be due to temperature changes, in particular from the reflective coating on the cantilever, which can result in bending of the cantilever [5]. This effect was mitigated by turning on the equipment some time before performing experiments, which let the thermals come to equilibrium in operating conditions. Additionally, the deflection zero-level was reset between each subsequent indentation.

V. SYSTEM IDENTIFICATION AND TUNING

In order to implement the parameter estimator, the cantilever dynamics (2) need to be known. In particular, the system parameters M, K, C need to be identified in order to implement w using (12).

The experiments were implemented on a commercial AFM (Park Systems XE-70) using a spherical carbon tip cantilever with 40 nm tip radius (B40_CONTR), operated in air.

A. System identification

The cantilever spring constant K was calibrated by the thermal noise method [45] with modifications from [5]. In this method, first, the power spectral density of the cantilever is recorded without any applied force. The spectral density is then fit to a Cauchy distribution near the first resonance mode. The mean square deflection $\langle D^2 \rangle$ can then be found through integration of the fit. Finally, the spring constant is found by using

$$K = \beta^* \frac{k_B T}{\langle D^2 \rangle} \qquad (47)$$

where $\beta^* = 0.817$ is a correction factor, k_B is the Boltzmann constant and T is the absolute temperature of the cantilever. The fit of the spectral density to the Cauchy distribution, from our experiments, can be seen in Fig. 7a.

In order to identify the cantilever effective mass and damping coefficient, the frequency response of the cantilever deflection was found by applying white noise to the piezo modulator. The resonance frequency of the first mode, ω_0, was then identified at peak magnitude. Furthermore, the effective mass was found using the relationship

$$M = \frac{K}{\omega_0^2}. \tag{48}$$

Finally, the transfer function was fitted to the frequency response data by adjusting C. A good fit near the resonance peak was emphasized, and the result is seen in Fig. 7b. Note that the cantilever is actuated from the base of the cantilever fixture, which excites additional dynamics. Self-actuated cantilevers are also available resulting in a cleaner frequency response [46].

The resulting system parameters are given by

$$K = 0.816 \,\text{N/m}, \qquad C = 7.86 \times 10^{-8} \,\text{Ns/m},$$
$$M = 8.42 \times 10^{-11} \,\text{kg}, \qquad f_0 = 15.7 \,\text{kHz}$$

with $\omega_0 = 2\pi f_0$.

Additionally, a calibration for the piezo modulator voltage-to-force ratio need to be determined. This was performed by applying a sinusoidal signal at cantilever resonance frequency and comparing the deflection response with the expected output from the previously found transfer function.

B. Estimator tuning

The parameter estimator needs to be appropriately tuned for the experimental conditions. The main tunables are β and $\mathbf{P}_0$. Here, β determines the bandwidth of the estimator, with very high values resulting in noisy estimates. The $\mathbf{P}_0$ matrix determines the level of trust in the initial conditions of the parameter estimates, with large values meaning low trust, and thus fast initial convergence.

The following values were determined which provided a reasonable bandwidth with low noise:

$$\beta = 50, \quad \mathbf{P}_0 = \text{diag}(5 \times 10^7, 1 \times 10^{18}).$$

Additionally, α was set to unity.

C. Estimation time interval

By using the results from Corollary 1, the estimation time during each indentation, for which the parameter error is guaranteed to be sufficiently small, can be found. However, the PE properties of the signal vector need to be known in order to apply the results. In the following, it is demonstrated how to find the desired time interval when using sample model $\mathcal{A}$, and the estimator tuning from the previous section.

Consider the applied sinusoidal cantilever modulation force (27). Assuming that the resulting cantilever deflection is dominated by a linear response, and that the cantilever is in contact with the sample, we have

$$\delta = A\sin(\omega_0 t + \varphi) + \bar{\delta} \tag{49}$$
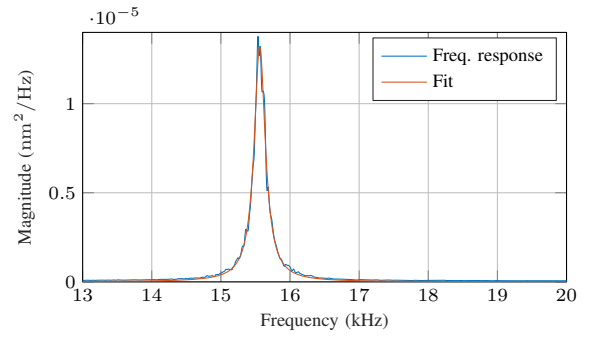
(a)
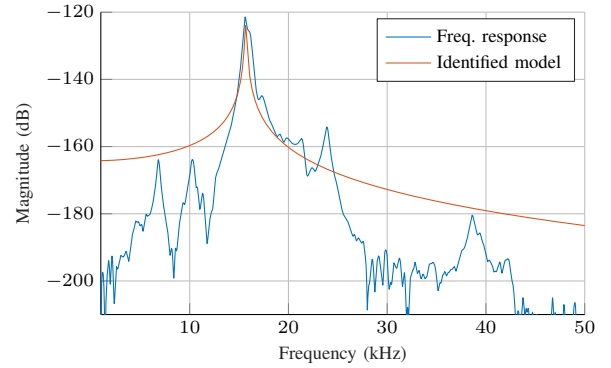
(b)

Fig. 7: System identification. (a) Cantilever spring constant calibration. (b) Cantilever frequency response and approximated second-order model, from piezo modulator to deflection.

for some amplitude A, phase φ, and mean depth $\bar{\delta} \geq A$. While nonlinear tip-sample interaction forces can induce a response at other frequencies, they would be substantially attenuated due to the strong resonance effect of the cantilever near ω_0. Thus, (49) should be a close approximation to the experimental situation. Inserting (49) into $\phi_{\mathcal{A}}$ from (14) gives the signal vector

$$\phi_{\mathcal{A}} = \begin{bmatrix} A\omega\cos(\omega_0 t + \varphi) & A\sin(\omega_0 t + \varphi) + \bar{\delta} \end{bmatrix}^T. \tag{50}$$

Next, consider the PE expression from (26) and define

$$\mathbf{S} \triangleq \frac{1}{T_{\text{p}}} \int_t^{t+T_{\text{p}}} \phi_{\mathcal{A}} \phi_{\mathcal{A}}^T d\tau. \tag{51}$$

By choosing

$$T_{\text{p}} = 2\pi\omega_0^{-1} \tag{52}$$

and using (50), it can be shown that the solution to (51) is given by

$$\mathbf{S} = \begin{bmatrix} \frac{1}{2}A^2\omega_0^2 & 0 \\ 0 & \frac{1}{2}A^2 + \bar{\delta}^2 \end{bmatrix}. \tag{53}$$

Thus, $\phi_{\mathcal{A}}$ is PE with level of excitation α_0 and α_1 given by

$$\alpha_0 = \min\left\{\tfrac{1}{2}A^2\omega_0^2, \tfrac{1}{2}A^2 + \bar{\delta}^2\right\} \tag{54}$$
$$\alpha_1 = \max\left\{\tfrac{1}{2}A^2\omega_0^2, \tfrac{1}{2}A^2 + \bar{\delta}^2\right\} \tag{55}$$

which satisfy the PE condition

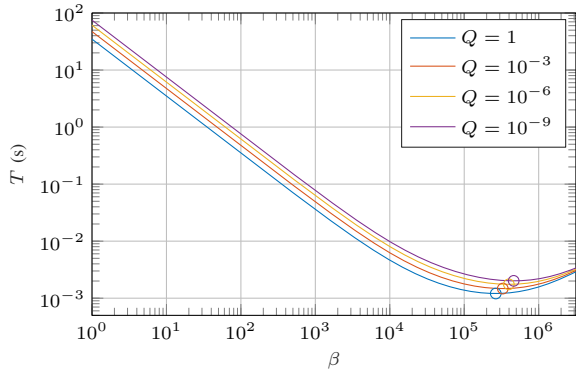$$\alpha_0\mathbf{I} \leq \mathbf{S} \leq \alpha_1\mathbf{I}. \tag{56}$$

Fig. 8: Minimum estimation time T which guarantees convergence of the parameter estimate error to within Q fraction of the initial error.

Thus, with the PE condition found, Corollary 1 can then be used to find the time interval T, within which the parameter error is guaranteed to be desirably small. First, the following properties can be determined by considering $\phi_{\mathcal{A}}$ from (50)

$$\bar{\phi}_{\mathcal{A}}^2 = A^2\omega^2 + \left(A + \bar{\delta}\right)^2, \quad \bar{m}_{\mathcal{A}}^2 = 1 + \bar{\phi}_{\mathcal{A}}^2, \qquad (57)$$

Using (29)-(34), the time interval can be plotted as a function of β at various values of Q, as seen in Fig. 8.

By using the tuned value of β, it was found that the time interval which guarantees that the estimator error has been reduced to $Q = 0.001\%$ of the initial value is given by

$$T = 1.13\,\text{s}. \qquad (58)$$

For the actual implementation, the time interval was rounded up to $1.2\,\text{s}$. This value was used as the time spent in the *Stationary* state during each indentation, see Fig. 6.

The analysis used to ultimately arrive at the value given in (58) is inherently conservative. Thus, the actual convergence of the parameters might occur at a faster rate. If a faster imaging procedure is desired, the time interval can be reduced by considering the rate of convergence achieved in simulations or experiments. For reference, we found in our own experiments that the time until convergence was around one-tenth of the value given in (58).

VI. EXPERIMENTAL RESULTS

The method was implemented on the commercial AFM (Park Systems XE-70) employed in the previous section, using the same cantilever (B40_CONTR). The AFM was connected to an embedded computer (dSpace DS1103) controlling all aspects of the operation. A Simulink program implements the necessary equations from the previous sections, as well as the scanning logic. The program was transferred to the embedded computer before operation.

The parameter estimator and demodulator was implemented online at a sampling rate of $200\,\text{kHz}$. The state machine and XYZ controller was run at a separate sampling rate of $1\,\text{kHz}$. This separation allows for faster sampling speed for the estimator. The XYZ controller was tuned for relatively low bandwidths, and its sampling rate was thus sufficient.

A. Two-component polymer film sample

The first experiment was performed to demonstrate the normal operating procedure of DIVE mode AFM, revealing spatially varying viscoelastic properties of the sample. A total of 30×30 indentations into a PS-LDPE-12M film sample were performed. This two-component polymer sample has specified elastic moduli of around $0.1\,\text{GPa}$ and $2\,\text{GPa}$ for the two components. The sample is especially suitable for measuring variations in elasticity due to its clear contrast between the two polymer components.

In this experiment, sample model $\mathcal{A}$ was used for online estimation of spring constants and damping coefficients. In order to find the elastic modulus, equation (8) was used offline. The results of the scan can be seen in Fig. 9. The contrast in elasticity between the two polymer components is clearly visible.

For each pixel in the scan results, the online estimator recursively estimates the spring constant and the damping coefficient. The vertical tip position and corresponding parameter estimates in the time-domain, during two subsequent indentations, are shown in Fig. 10. The first indentation is located in the softer region of the sample, while the second indentation near the stiffer region. This results in the first indentation going deeper, as seen in Fig. 10a. Since the second indentation does not reach deep into the sample, it is consequently more prone to noise in the depth estimate, resulting in somewhat more noisy parameter estimates as seen in Fig. 10b. To mitigate such noise, it is emphasized that the spring constant and tip radius of the cantilever used, need to be suitable for the sample being investigated. A very soft cantilever will deflect too much before it sufficiently indents the sample, while a very stiff cantilever will indent the sample without sufficiently deflecting and can cause damage.

B. Homogeneous gel sample

In the second set of experiments, a soft gel sample (PDMS-SOFT-1-12M) was used with a specified elastic modulus of about $2.5\,\text{MPa}$. Four experiments at 20×20 resolution were performed in order to compare sample model $\mathcal{A}$ and $\mathcal{B}$ at different indentation depths, $100\,\text{nm}$ and $250\,\text{nm}$, respectively. The resulting identified spring constants (sample model $\mathcal{A}$) and elastic moduli (sample model $\mathcal{B}$) are shown in Fig. 11.

The mean of the identified parameters from each experiment is given in Table I. The identified elastic modulus is close to the specified value of $2.5\,\text{MPa}$. If the sample perfectly complies with the Hertz model, then the elastic modulus should be invariant with regards to the indentation depth. However, the results indicate some difference at the two depths. This suggests that the Hertz model is not completely descriptive for the experimental setup. In particular, the indentation is large compared to the radius of the cantilever, which violates the assumption of small indentations. This could be mitigated by using a cantilever with a larger tip radius, or lower spring constant. Additionally, adhesion effects could be large, something which is further discussed in the next experiment.

Note that the difference in the mean spring constant is larger than for the elastic modulus. This can be used as an argument
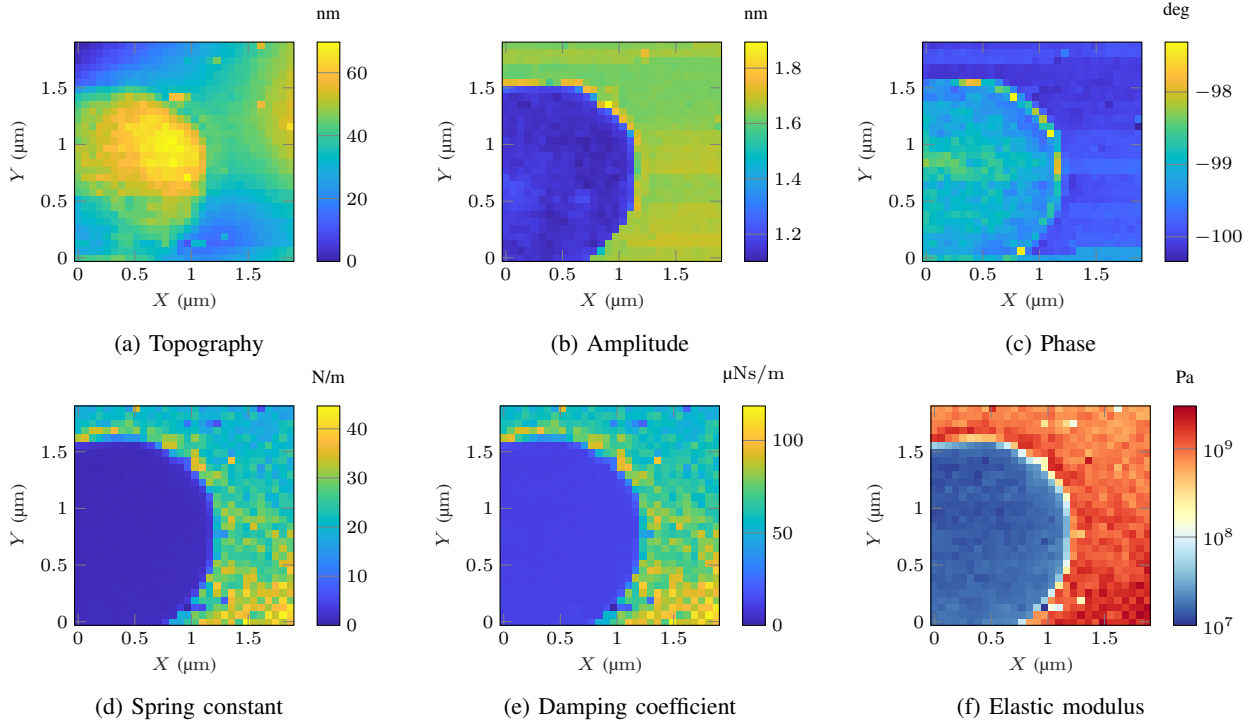
(a) Topography

(b) Amplitude

(c) Phase

(d) Spring constant

(e) Damping coefficient

(f) Elastic modulus

Fig. 9: AFM experiment for a two-component polymer sample.

(a) Vertical tip position
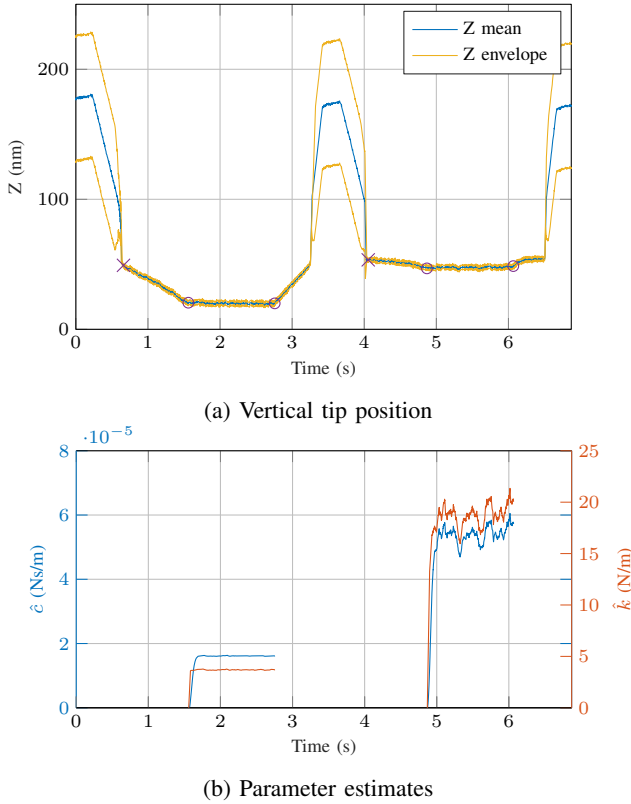
(b) Parameter estimates

Fig. 10: Tip position (a) and parameter estimation (b) during two subsequent indentations into the two-component polymer sample. In (a), crosses '×' mark contact detection point (topography), while within the circles '○' the stationary state is active and sample parameters are estimated.

TABLE I: Depth versus elasticity.

Indentation	Spring constant	Elastic modulus
$100\,\mathrm{nm}$	$0.335\,\mathrm{N/m}$	$2.73\,\mathrm{MPa}$
$250\,\mathrm{nm}$	$0.435\,\mathrm{N/m}$	$2.31\,\mathrm{MPa}$
Difference	$26.0\,\%$	$16.7\,\%$

in favor of implementation of the Hertz sample model $\mathcal{B}$, and demonstrates the necessity of a nonlinear sample model.

For many soft, biological materials it is not possible to calculate the elastic modulus [40], as they do not even approximately behave in accordance with Hooke's law or its nonlinear variants, which is the basis of the elastic models presented in this article. For such materials, a more suitable sample model could be developed, and used in the modeling and identification approach as presented.

C. Time-varying estimation

Since the approach presented in this article uses a recursive parameter estimation scheme, the time-varying nature of the parameters can be recorded. This can be demonstrated by performing a single indentation into a soft sample. If the sample complies with the Hertz model, then the spring constant from sample model $\mathcal{A}$ should increase with increasing indentation depth. Thus, if the cantilever tip is lowered and raised again, experimental results should demonstrate time-varying parameters.

This experiment was performed on the same gel sample as previous (PDMS-SOFT-1-12M). During the experiment, the cantilever was lowered until it reached some specified depth
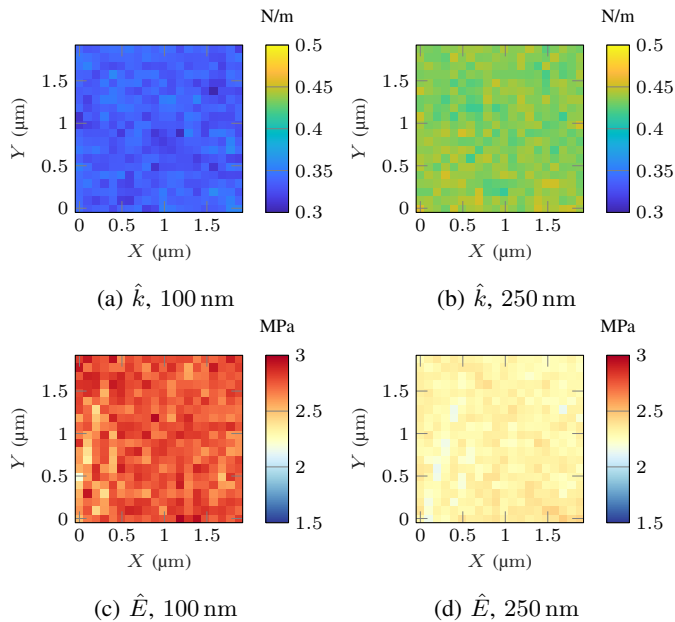
(a) $\hat{k}$, 100 nm (b) $\hat{k}$, 250 nm

(c) $\hat{E}$, 100 nm (d) $\hat{E}$, 250 nm

Fig. 11: Four AFM experiments demonstrating spring constant (sample model $\mathcal{A}$) versus elastic modulus (sample model $\mathcal{B}$) identification at different indentation depths on a homogeneous gel sample.

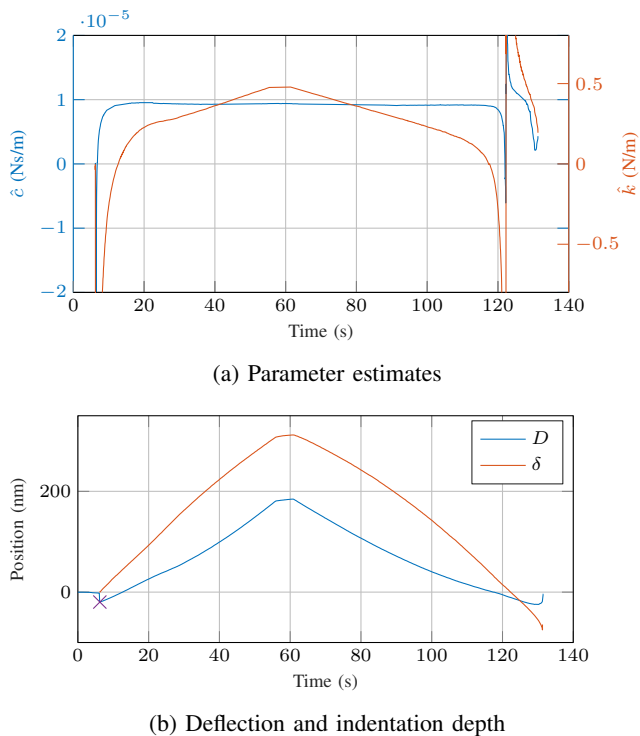(a) Parameter estimates

(b) Deflection and indentation depth

Fig. 12: Time-varying parameter estimates. The estimated spring constant is shown to change with the indentation depth. Unmodeled adhesion effects give rise to unreliable results at the start and end of the experiment.

into the sample, then raised again. Throughout the whole procedure, while the tip was in contact with the sample, the parameter estimator was enabled. The experiment was implemented at a slow vertical speed, to make sure that the parameter estimates were accurate. The cantilever and experimental setup from the previous experiments have otherwise been used.

The results of the experiment are given in Fig. 12. The parameter estimates as shown in Fig. 12a demonstrate that the spring constant generally increases with increasing indentation depth as expected, and decreases as the tip is raised again. Thus, proper estimation of time-varying parameters by using the presented approach is demonstrated.

The results also demonstrate several effects due to *adhesion and deformation* that should be considered when performing experiments:

1) After initial contact: Initially after contact, the spring constant estimates become negative. Negative spring constants make little physical sense unless one considers the effect of adhesion. As the tip approaches the sample, attractive adhesion forces pull the tip onto the sample, resulting in a negative cantilever deflection (Fig. 12b) which is interpreted as negative interaction forces by the parameter estimator. The best fit of the positive indentation depth signal onto the negative cantilever deflection using the sample models implemented, results in negative parameter estimates.

2) Raising the cantilever: A similar effect is seen towards the end of the experiment, just before the tip is freed from the sample. As the tip is raised, adhesion forces will make the sample stick to the cantilever tip. This could also result in deformation of the sample, by raising it towards the tip as it is lifted. For these reasons, in the experiment, at some point the indentation depth becomes zero and then negative. As it approaches zero depth, the spring constant estimate grows toward either positive or negative infinity, depending on the net force experienced by the cantilever. Generally, the sample model and estimates in the adhesive regime is thus invalid.

These effects could explain the difference of the elastic modulus at different depths in the previous experiment. In order to mitigate the effect of adhesion, the sample model could be modified to include adhesion, such as by employing the Johnson-Kendall-Roberts (JKR) or Derjaguin-Muller-Toporov (DMT) contact models [8].

VII. CONCLUSIONS

A model-based identification technique is presented for determining spatially resolved nanomechanical properties in AFM. Both the cantilever and sample behavior is described by dynamic models. The cantilever dynamics are assumed known by identifying its parameters before performing the experiments, while the sample dynamics incorporate the unknown parameters to be identified. A recursive least squares estimator is used for identification of the sample parameters.

Employing a recursive estimator has several advantages over comparable techniques. First, it allows online identification of the nanomechanical properties, enabling the operator to see real-time conditions. Secondly, it allows the determination

of time-varying changes of the parameters as demonstrated by the experiments. This could be useful by itself, such as for observing changing conditions in cells or other biological material. Finally, observing such time-varying changes could reveal erroneous conditions or unmodeled dynamics, as this could dramatically affect the estimated parameters. An example of this is seen in the last experiment, where negative and diverging spring constant estimates are seen near the beginning and end of the experiment. This is believed primarily to occur due to unmodeled adhesion effects.

Furthermore, we have derived an analytical expression for the estimation time interval of the recursive least squares estimator. Within this time interval, the parameter error is guaranteed to have been reduced to any given fraction of the initial error. The time interval can be determined a priori, and spending this length of time at each indentation point then guarantees that the parameters will converge to any desired accuracy. This is verified by the experiments, where the parameters are seen to converge within the determined time interval.

Two sample models are developed and implemented for this approach – a linear spring-damper model and a nonlinear Hertz model. It is demonstrated that only minor modifications are needed to switch between the models. The experiments show the Hertz model to be a better match. However, some materials may not be well described by this model, and it is then a clear advantage of the proposed modeling and identification approach that the sample model can be exchanged for a more suitable dynamic model.

ACKNOWLEDGMENT

REFERENCES

[1] D. Y. Abramovitch, S. B. Andersson, L. Y. Pao, and G. Schitter, "A Tutorial on the Mechanisms, Dynamics, and Control of Atomic Force Microscopes," in *Proc. 2007 American Control Conference*, New York, USA, 2007, pp. 3488–3502.

[2] D. J. Müller and Y. F. Dufrêne, "Atomic force microscopy: a nanoscopic window on the cell surface." *Trends in cell biology*, vol. 21, no. 8, pp. 461–469, 2011.

[3] K. Haase and A. E. Pelling, "Investigating cell mechanics with atomic force microscopy," *Journal of The Royal Society Interface*, vol. 12, no. 104, 2015.

[4] F. Javadpour, M. Moravvej Farshi, and M. Amrein, "Atomic-Force Microscopy: A New Tool for Gas-Shale Characterization," *Journal of Canadian Petroleum Technology*, vol. 51, no. 04, pp. 236–243, 2012.

[5] H.-J. Butt, B. Cappella, and M. Kappl, "Force measurements with the atomic force microscope: Technique, interpretation and applications," *Surface Science Reports*, vol. 59, no. 1-6, pp. 1–152, 2005.

[6] P. Polyakov, C. Soussen, J. Duan, J. F. L. Duval, D. Brie, and G. Francius, "Automated Force Volume Image Processing for Biological Samples," *PLOS ONE*, vol. 6, no. 4, pp. 1–19, 2011.

[7] I. Sokolov, M. E. Dokukin, and N. V. Guz, "Method for quantitative measurements of the elastic modulus of biological cells in AFM indentation experiments," *Methods*, vol. 60, no. 2, pp. 202–213, 2013.

[8] K. K. M. Sweers, M. L. Bennink, and V. Subramaniam, "Nanomechanical properties of single amyloid fibrils," *Journal of Physics: Condensed Matter*, vol. 24, no. 24, p. 243101, 2012.

[9] M. E. Dokukin and I. Sokolov, "Quantitative Mapping of the Elastic Modulus of Soft Materials with HarmoniX and PeakForce QNM AFM Modes," *Langmuir*, vol. 28, no. 46, pp. 16 060–16 071, 2012.

[10] O. Sahin, S. Magonov, C. Su, C. F. Quate, and O. Solgaard, "An atomic force microscope tip designed to measure time-varying nanomechanical forces." *Nature nanotechnology*, vol. 2, no. 8, pp. 507–14, 2007.

[11] Y. M. Efremov, W.-H. Wang, S. D. Hardy, R. L. Geahlen, and A. Raman, "Measuring nanoscale viscoelastic parameters of cells directly from AFM force-displacement curves," *Scientific Reports*, vol. 7, no. 1, p. 1541, 2017.

[12] B. R. Brückner, H. Nöding, and A. Janshoff, "Viscoelastic Properties of Confluent MDCK II Cells Obtained from Force Cycle Experiments," *Biophysical Journal*, vol. 112, no. 4, pp. 724–735, 2017.

[13] R. Garcia and R. Perez, "Dynamic atomic force microscopy methods," *Surface science reports*, vol. 47, no. 6-8, pp. 197–301, 2002.

[14] F. J. Giessibl, "Advances in atomic force microscopy," *Reviews of modern physics*, vol. 75, no. 3, pp. 949–983, 2003.

[15] N. A. Burnham, O. P. Behrend, F. Oulevey, G. Gremaud, P.-J. Gallo, D. Gourdon, E. Dupas, A. J. Kulik, H. M. Pollock, and G. A. D. Briggs, "How does a tip tap?" *Nanotechnology*, vol. 8, no. 2, pp. 67–75, 1997.

[16] M. Radmacher, R. W. Tillmann, and H. E. Gaub, "Imaging viscoelasticity by force modulation with the atomic force microscope." *Biophysical journal*, vol. 64, no. 3, pp. 735–742, 1993.

[17] A. Raman, S. Trigueros, A. Cartagena, A. P. Z. Stevenson, M. Susilo, E. Nauman, and S. A. Contera, "Mapping nanomechanical properties of live cells using multi-harmonic atomic force microscopy." *Nature nanotechnology*, vol. 6, no. 12, pp. 809–14, 2011.

[18] A. X. Cartagena-Rivera, W.-H. Wang, R. L. Geahlen, and A. Raman, "Fast, multi-frequency, and quantitative nanomechanical mapping of live cells using the atomic force microscope," *Scientific Reports*, vol. 5, p. 11692, 2015.

[19] E. T. Herruzo, A. P. Perrino, and R. Garcia, "Fast nanomechanical spectroscopy of soft matter," *Nature communications*, vol. 5, p. 3126, 2014.

[20] R. Hillenbrand, M. Stark, and R. Guckenberger, "Higher-harmonics generation in tapping-mode atomic-force microscopy: Insights into the tip-sample interaction," *Applied Physics Letters*, vol. 76, no. 23, pp. 3478–3480, 2000.

[21] F. J. Giessibl, "Higher-harmonic atomic force microscopy," *Surface and Interface Analysis*, vol. 38, no. 12-13, pp. 1696–1701, 2006.

[22] R. W. Stark and W. M. Heckl, "Higher harmonics imaging in tapping-mode atomic-force microscopy," *Review of Scientific Instruments*, vol. 74, no. 12, pp. 5111–5114, 2003.

[23] O. Sahin, C. F. Quate, O. Solgaard, and F. J. Giessibl, "Higher Harmonics and Time-Varying Forces in Dynamic Force Microscopy," in *Springer Handbook of Nanotechnology*, B. Bhushan, Ed. Springer Berlin Heidelberg, 2010, pp. 711–729.

[24] T. Li and Q. Zou, "Simultaneous Topography Imaging and Broadband Nanomechanical Property Mapping using Atomic Force Microscope," in *Proc. 2017 American Control Conference*, Seattle, USA, 2017, pp. 795–800.

[25] Y. F. Dufrêne, T. Ando, R. Garcia, D. Alsteens, D. Martinez-Martin, A. Engel, C. Gerber, and D. J. Müller, "Imaging modes of atomic force microscopy for application in molecular and cell biology," *Nature Nanotechnology*, vol. 12, no. 4, pp. 295–307, 2017.

[26] M. R. Ragazzon, J. T. Gravdahl, and M. Vagia, "Viscoelastic properties of cells: Modeling and identification by atomic force microscopy," *Mechatronics*, 2017, in press, available: https://doi.org/10.1016/j.mechatronics.2017.09.011.

[27] M. R. P. Ragazzon, M. Vagia, and J. T. Gravdahl, "Cell Mechanics Modeling and Identification by Atomic Force Microscopy," in *Proc. 7th IFAC Symposium on Mechatronic Systems*, Loughborough, UK, 2016.

[28] M. R. P. Ragazzon and J. T. Gravdahl, "Imaging Topography and Viscoelastic Properties by Constant Depth Atomic Force Microscopy," in *Proc. IEEE Multi-Conference on Systems and Control*, Buenos Aires, Argentina, 2016.

[29] M. R. P. Ragazzon, J. T. Gravdahl, and K. Y. Pettersen, "Exponential Convergence Bounds in Least Squares Estimation: Identification of Viscoelastic Properties in Atomic Force Microscopy," in *Proc. IEEE Conference on Control Technology and Applications*, Kohala Coast, Hawai'i, USA, 2017.

[30] S. Devasia, E. Eleftheriou, and S. O. R. Moheimani, "A Survey of Control Issues in Nanopositioning," *IEEE Transactions on Control Systems Technology*, vol. 15, no. 5, pp. 802–823, 2007.

[31] A. A. Eielsen, J. T. Gravdahl, and K. Y. Pettersen, "Adaptive feedforward hysteresis compensation for piezoelectric actuators," *Review of Scientific Instruments*, vol. 83, no. 8, p. 085001, 2012.

[32] J. Å. Stakvik, M. R. P. Ragazzon, A. A. Eielsen, and J. T. Gravdahl, "On Implementation of the Preisach Model: Identification and Inversion for Hysteresis Compensation," *Modeling, Identification and Control*, vol. 36, no. 3, pp. 133–142, 2015.

[33] A. A. Eielsen, M. Vagia, J. T. Gravdahl, and K. Y. Pettersen, "Damping and Tracking Control Schemes for Nanopositioning," *IEEE/ASME Transactions on Mechatronics*, vol. 19, no. 2, pp. 432–444, 2013.

[34] A. Sebastian and S. M. Salapaka, "Design methodologies for robust nano-positioning," *IEEE Transactions on Control Systems Technology*, vol. 13, no. 6, pp. 868–876, 2005.

[35] Y. K. Yong, K. Liu, and S. O. R. Moheimani, "Reducing cross-coupling in a compliant XY nanopositioner for fast and accurate raster scanning," *IEEE Transactions on Control Systems Technology*, vol. 18, no. 5, pp. 1172–1179, 2010.

[36] A. J. Fleming and K. K. Leang, *Design, Modeling and Control of Nanopositioning Systems*. Cham, Switzerland: Springer, 2014.

[37] B. Bhushan and O. Marti, "Scanning Probe Microscopy - Principle of Operation, Instrumentation, and Probes," in *Springer Handbook of Nanotechnology*, B. Bhushan, Ed. Springer Berlin Heidelberg, 2010, pp. 573–617.

[38] D. Sarid, *Scanning force microscopy*. New York: Oxford University Press, 1994.

[39] P. Carl and H. Schillers, "Elasticity measurement of living cells with an atomic force microscope: data acquisition and processing," *Pflügers Archiv - European Journal of Physiology*, vol. 457, no. 2, pp. 551–559, 2008.

[40] S. Kasas and G. Dietler, "Probing nanomechanical properties from biomolecules to living cells," *Pflügers Archiv - European Journal of Physiology*, vol. 456, no. 1, pp. 13–27, 2008.

[41] P. A. Ioannou and J. Sun, *Robust adaptive control*. Upper Saddle River, NJ: Prentice Hall, 1996.

[42] B. D. O. Anderson and R. M. Johnstone, "Adaptive systems and time varying plants," *International Journal of Control*, vol. 37, no. 2, pp. 367–377, 1983.

[43] M. R. P. Ragazzon, M. G. Ruppert, D. M. Harcombe, A. J. Fleming, and J. T. Gravdahl, "Lyapunov Estimator for High-Speed Demodulation in Dynamic Mode Atomic Force Microscopy," *IEEE Transactions on Control Systems Technology*, vol. 26, no. 2, pp. 765–772, 2018.

[44] M. G. Ruppert, D. M. Harcombe, M. R. P. Ragazzon, S. O. R. Moheimani, and A. J. Fleming, "A review of demodulation techniques for amplitude-modulation atomic force microscopy," *Beilstein Journal of Nanotechnology*, vol. 8, no. 1, pp. 1407–1426, 2017.

[45] J. L. Hutter and J. Bechhoefer, "Calibration of atomic-force microscope tips," *Review of Scientific Instruments*, vol. 64, no. 7, p. 1868, 1993.

[46] S. R. Manalis, S. C. Minne, A. Atalar, and C. F. Quate, "High-speed atomic force microscopy using an integrated actuator and optical lever detection," *Review of Scientific Instruments*, vol. 67, no. 9, pp. 3294–3297, 1996.